Article | Open Access

Energy Materials

Zheng et al. Energy Mater. 2026, 6, 600122 DOI:10.20517/energymater.2026.217

Robust $CoRuO_x$ oxide catalysts with broad electrolyte compatibility toward superior hydrogen evolution

Qianqian Zheng[1], Yang Li[1], Chunling Lu[1], Manoko S. Maubane-Nkadimeng[3], Tao Feng[2,*], Bingbing Niu[1,*]

Keywords:
Hydrogen evolution reaction, stability, electrolyte adaptability, overpotential

Citation: Zheng, Q.; Li, Y.; Lu, C.; Maubane-Nkadimeng, M. S.; Feng, T.; Niu, B. Robust $CoRuO_x$ oxide catalysts with broad electrolyte compatibility toward superior hydrogen evolution. *Energy Mater.* **2026**, *6*, 600122. https://dx.doi.org/10.20517/energymater.2026.217

Received: 9 Jul 2026
First Decision: 23 Jul 2026
Revised: 29 Aug 2026
Accepted: 3 Sep 2026
Published: 22 Sep 2026

Academic Editor:
Ho Won Jang
Copy Editor:
Fangling Lan
Production Editor:
Fangling Lan

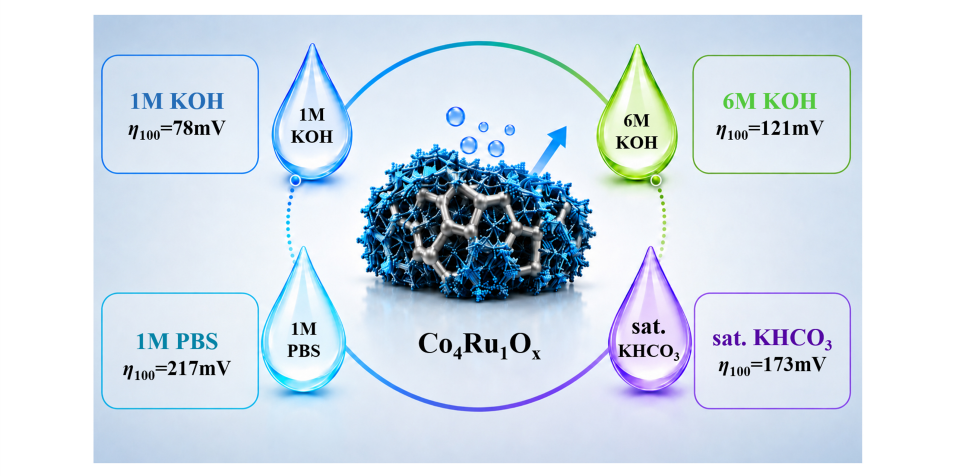

Abstract

Developing hydrogen evolution reaction (HER) electrocatalysts that combine high activity with reliable operation in different electrolytes remains important for clean-hydrogen and electrochemical-energy technologies. In this study, CoRu composite oxides with adjustable Co/Ru molar ratios were formed in situ on nickel foam through co-precipitation and subsequent high-temperature calcination, and their HER behavior was examined in alkaline, neutral, and near-neutral media. $Co_4Ru_1O_x$ showed the good activity and durability. In 1 M KOH, current densities of 100, 300, and 700 mA cm^{-2} were obtained at overpotentials of 78, 127, and 196 mV, respectively; the corresponding Tafel slope was 21.64 mV dec^{-1}. The electrode also operated for 200 h in both 1 and 6 M KOH. When incorporated into a membrane electrode assembly electrolyzer, $Co_4Ru_1O_x$||NF sustained overall water splitting at 100 mA cm^{-2} for 200 h. In 1 M phosphate buffer solution, only 16 mV was needed to deliver 10 mA cm^{-2}, and stable operation was again maintained for 200 h. High-current HER activity was also obtained in saturated $KHCO_3$, while a Zn-CO_2 cell using this catalyst reached a maximum power density of 9.6 mW cm^{-2}. Collectively, these findings identify

[1]School of Science, University of Science and Technology Liaoning, Anshan 114051, Liaoning, China.
[2]Department of Materials Science and Engineering, Southern University of Science and Technology, Shenzhen 518055, Guangdong, China.
[3]Microscopy and Microanalysis Unit, School of Chemistry, University of Witwatersrand, Johannesburg 2050, South Africa.

*Correspondence to: Dr. Tao Feng, Department of Materials Science and Engineering, Southern University of Science and Technology, Shenzhen 518055, Guangdong, China. E-mail: fengt@sustech.edu.cn; Dr. Bingbing Niu, School of Science, University of Science and Technology Liaoning, Anshan 114051, Liaoning, China. E-mail: niubb@ustl.edu.cn

$Co_4Ru_1O_x$ as a multifunctional HER electrode suited to several electrochemical environments.

INTRODUCTION

Rising energy consumption and worsening environmental pollution have intensified interest in hydrogen as a clean energy vector because it has a high mass-specific energy content and produces only water upon combustion[1-3]. Water electrolysis powered by renewable electricity can generate high-purity hydrogen through a sustainable pathway[4]. During the hydrogen evolution reaction (HER), water adsorbs and dissociates before hydrogen intermediates form and subsequently desorb. Catalysts that retain both activity and stability across dissimilar electrolytes are therefore required for efficient hydrogen production and practical energy-conversion systems[5].

Platinum catalysts provide fast HER kinetics at small overpotentials, but their broader use is limited by the scarcity and high cost of Pt[4,6]. Prolonged operation can also promote particle agglomeration and the loss of active sites, thereby compromising durability and impeding large-scale electrochemical hydrogen production[7,8]. Ruthenium is a less expensive platinum-group metal with considerable HER activity and has consequently been studied as an alkaline-media substitute for Pt[9,10]. Even so, single-phase Ru catalysts may use the noble metal inefficiently and may lack structural robustness. Combining Ru with cobalt oxides offers a route to lower Ru loading while exploiting cooperative effects to improve activity and stability[11-13]. The benefits of such Ru-Co oxides in alkaline HER have been demonstrated previously. Zhang *et al.*, for example, derived the Ru-Co_3O_4-NiO-NF heterostructure from a metal-organic framework[12]. In 1 M KOH, this catalyst required 44 mV at 10 mA cm^{-2} and 115 mV at 100 mA cm^{-2}. It outperformed most reported Ru-Co catalysts and commercial Pt/C in that study and remained stable during a 60 h test at high current density. Ren *et al.* later prepared a MOF-derived RuO_2-Co_3O_4 bimetallic oxide in which interactions between the two oxide components modified the local electronic structure and promoted interfacial charge redistribution[13].

Although Ru-Co-based oxides have demonstrated promising HER performance in alkaline media[13], recent studies have begun to explore their activity under broader pH conditions, highlighting the additional kinetic challenges posed by neutral and near-neutral electrolytes[14,15]. Nevertheless, systematic investigations of Ru-Co-based oxides across distinct electrolyte environments, particularly buffered and bicarbonate-containing media, remain limited. In neutral or buffered media, HER kinetics are governed by water dissociation, buffer-assisted proton transfer, local pH variation, and interfacial mass transport and differ markedly from those in strongly alkaline electrolytes[16-18]. Therefore, evaluating catalysts beyond conventional alkaline KOH is essential for clarifying their adaptability to different proton-transfer and interfacial reaction environments[18,19]. Kim *et al.* proposed aqueous Zn/Al-CO_2 systems that exploit CO_2-induced acidity to achieve simultaneous electricity generation and H_2 production, using a separated alkaline anodic compartment and a saturated $KHCO_3$ cathodic environment[20]. In this metal-CO_2 configuration, a saturated $KHCO_3$ electrolyte creates a bicarbonate-rich cathodic environment, where local acidity is generated by continuous CO_2 feeding. The HER catalyst at the cathode must not only accelerate proton reduction for efficient H_2 generation but also maintain catalytic activity and interfacial stability during the accompanying CO_2 mineralization process. This process involves HCO_3^-/CO_3^{2-} interconversion, local pH fluctuation, competitive adsorption, and carbonate precipitation at the reactive interface. Therefore, the half-cell tests in saturated $KHCO_3$ provide a more realistic assessment of the catalyst under metal-CO_2 cathodic conditions. Integration into a full metal-CO_2 cell further verifies the catalyst's ability to promote hydrogen production and enhance the overall power output.

Here, a multifunctional Ru-Co oxide catalyst was fabricated on nickel foam (NF) by co-precipitation and heat treatment. We then assessed its electrochemical response in 1 M KOH, 6 M KOH, saturated $KHCO_3$, and 1 M phosphate buffer solution (PBS). The catalyst showed strong and durable HER activity in both KOH

concentrations; it also performed well in PBS and showed utility for a metal-CO_2 configuration in saturated $KHCO_3$. These properties reflect cooperation between the Ru and Co oxide components, rapid mass and charge transfer through the three-dimensional conductive NF scaffold, and the availability of numerous surface sites. Beyond alkaline testing, the study establishes how the HER behavior of Ru-Co oxides changes with electrolyte environment. Relating activity to interfacial water activation, charge-transfer behavior, and electrolyte-controlled proton delivery provides a basis for designing durable HER catalysts with broad electrolyte tolerance.

EXPERIMENTAL

Chemicals

Analytical-grade ruthenium chloride hydrate ($RuCl_3 \cdot xH_2O$), cobalt(II) chloride hexahydrate ($CoCl_2 \cdot 6H_2O$), potassium bicarbonate ($KHCO_3$), anhydrous ethanol (C_2H_5OH), urea ($CO(NH_2)_2$), 1 M PBS (pH 7.0), ethylene glycol ($C_2H_6O_2$), hydrochloric acid (HCl, 36-38 wt%), and potassium hydroxide (KOH) were obtained from Aladdin. NF was obtained from Shanghai Jiaqingyuan Co., Ltd. Each chemical was employed as received, without an additional purification step.

Synthesis of $CoRuO_x$

$CoRuO_x$ electrocatalysts were deposited directly on NF by co-precipitation and then calcined. Before deposition, a 1 cm × 2 cm NF piece was sonicated for 10 min in 40 mL of 3 M HCl to strip the native oxide layer. It was subsequently sonicated in 40 mL of anhydrous ethanol for 3 min, washed repeatedly with deionized water until neutral, and dried at ambient temperature.

$RuCl_3 \cdot xH_2O$ and $CoCl_2 \cdot 6H_2O$ were used as the Ru and Co sources, respectively. To prepare $Co_1Ru_1(OH)_x$, 0.0414 g (0.2 mmol) of $RuCl_3 \cdot xH_2O$, 0.0476 g (0.2 mmol) of $CoCl_2 \cdot 6H_2O$, and 0.012 g (0.2 mmol) of urea were dispersed in 40 mL of ethylene glycol by sonication. The same protocol was applied to $Co_2Ru_1(OH)_x$, $Co_3Ru_1(OH)_x$, $Co_4Ru_1(OH)_x$, and $Co_5Ru_1(OH)_x$. In these syntheses, the Ru precursor was kept at 0.0414 g (0.2 mmol), whereas the mass of $CoCl_2 \cdot 6H_2O$ was set to 0.0952, 0.143, 0.1903, and 0.238 g to obtain Co/Ru molar ratios of 2:1, 3:1, 4:1, and 5:1. A Co-only solution was prepared by sonicating $CoCl_2 \cdot 6H_2O$ (0.1903 g, 0.8 mmol) and urea (0.012 g, 0.2 mmol) in 40 mL of ethylene glycol, corresponding to the CoO_x sample. The corresponding Ru-only solution contained $RuCl_3 \cdot xH_2O$ (0.0414 g, 0.2 mmol) and urea (0.012 g, 0.2 mmol) in the same volume of ethylene glycol, corresponding to the RuO_x sample.

The cleaned NF was placed vertically in each precursor solution, which was maintained at 95 °C for 12 h. The recovered specimens were alternately rinsed three times with anhydrous ethanol and deionized water to eliminate residual ions and weakly adsorbed material, followed by air drying at room temperature. The hydroxide intermediates were labeled $Co_1Ru_1(OH)_x$, $Co_2Ru_1(OH)_x$, $Co_3Ru_1(OH)_x$, $Co_4Ru_1(OH)_x$, $Co_5Ru_1(OH)_x$, $Co(OH)_x$, and $Ru(OH)_x$. They were placed in a crucible, heated at 2 °C min^{-1} to 300 °C, and calcined for 2 h. The products were denoted $Co_1Ru_1O_x$, $Co_2Ru_1O_x$, $Co_3Ru_1O_x$, $Co_4Ru_1O_x$, $Co_5Ru_1O_x$, CoO_x, and RuO_x, respectively. For electrochemical testing, a 1 cm × 1 cm catalyst-coated region was exposed to the electrolyte; the other 1 cm × 1 cm region was insulated and attached to the electrode clip. Reported current densities were normalized to the 1.0 cm^2 exposed geometric area.

Material characterizations

Sample morphology was examined by scanning electron microscopy (SEM, JSM-6701F, JEOL, Japan) at 5 kV. Transmission electron microscopy and high-resolution TEM (TEM/HRTEM, JEM-2100F, JEOL, Japan; 200 kV) were used to resolve the nanoscale and crystallographic features, while associated energy-

dispersive X-ray spectroscopy (EDS) maps provided elemental distributions. Surface composition and chemical states were analyzed by X-ray photoelectron spectroscopy (XPS, AXIS ULTRA DLD, Kratos Analytical, UK) using monochromatic Al Kα radiation (hυ = 1,486.6 eV) at 15 kV and 10 mA. Binding energies were referenced to the C 1s signal at 284.8 eV. Raman measurements employed a LabRAM HR Evolution system (HORIBA Scientific, France), a 473 nm laser, and a 600 grooves mm^{-1} grating. X-ray absorption fine-structure (XAFS) data spanning 4.5-20 keV were acquired on a SuperXAFS-H3000 benchtop hard X-ray absorption spectrometer (Shanghai Institute of Applied Physics, CAS, China). Fourier-transform infrared spectra were collected with a Vertex 80 Fourier Transform Infrared Spectroscopy (FTIR) instrument (Bruker, Germany).

Electrocatalytic measurements

Electrochemical measurements were performed using a CS350M workstation from CH Instruments. Catalyst-coated NF with a 1 cm^2 exposed area was the working electrode for HER testing in KOH; Hg/HgO and graphite were used as the reference and counter electrodes, respectively. Except for the potentials monitored directly during durability experiments, all measured potentials were converted to the reversible hydrogen electrode (RHE) scale. For a Hg/HgO electrode filled with 1 M KOH, the conversion followed Ref.[21]:

$$E_{vs.RHE} = E_{vs.Hg/HgO} + E^{\theta}_{Hg/HgO} + 0.059 \times pH \quad (1)$$

Potentials measured with an Ag/AgCl reference electrode containing saturated KCl were converted as described in Ref.[22]:

$$E_{vs.RHE} = E_{vs.Ag/AgCl} + E^{\theta}_{Ag/AgCl} + 0.059 \times pH \quad (2)$$

The measured pH values were 14, 7, and 8 for 1 M KOH, 1 M PBS, and saturated $KHCO_3$, respectively.

Linear sweep voltammograms were collected at 5 mV s^{-1} with 90% iR compensation. To estimate the electrochemical double-layer capacitance (C_{dl}), cyclic voltammograms in 1 M KOH were obtained at 10, 20, 40, 60, 80, 100, and 120 mV s^{-1}. The electrochemical surface area (ECSA) was then determined from C_{dl} using:

$$\mathrm{ECSA} = \left(\frac{C_{dl \times S}}{C_s}\right) \quad (3)$$

Here, S is the geometric area of the working electrode, and C_s is the specific capacitance assigned to an ideally smooth surface. A C_s value of 40 μF cm^{-2}, selected from prior electrochemical reports, was used in this study[23]. For 1 M PBS and saturated $KHCO_3$, CV data were collected at 20, 40, 60, 80, and 100 mV s^{-1}.

The durability of $Co_4Ru_1O_x$ was evaluated using a direct-current power supply for 200 h. The starting current density was -100 mA cm^{-2} in 1 and 6 M KOH and -10 mA cm^{-2} in 1 M PBS. Overall water splitting was evaluated in a membrane electrode assembly (MEA) containing $Co_4Ru_1O_x$ as the cathode and NF as the anode; its linear sweep voltammetry (LSV) curve was recorded at 50 mV s^{-1}. For Zn-CO_2 testing, Zn foil and $Co_4Ru_1O_x$ served as the anode and cathode, respectively, under continuous CO_2 supply. Polarization data were acquired at 50 mV s^{-1}, and the overpotentials were derived from RHE-converted potentials.

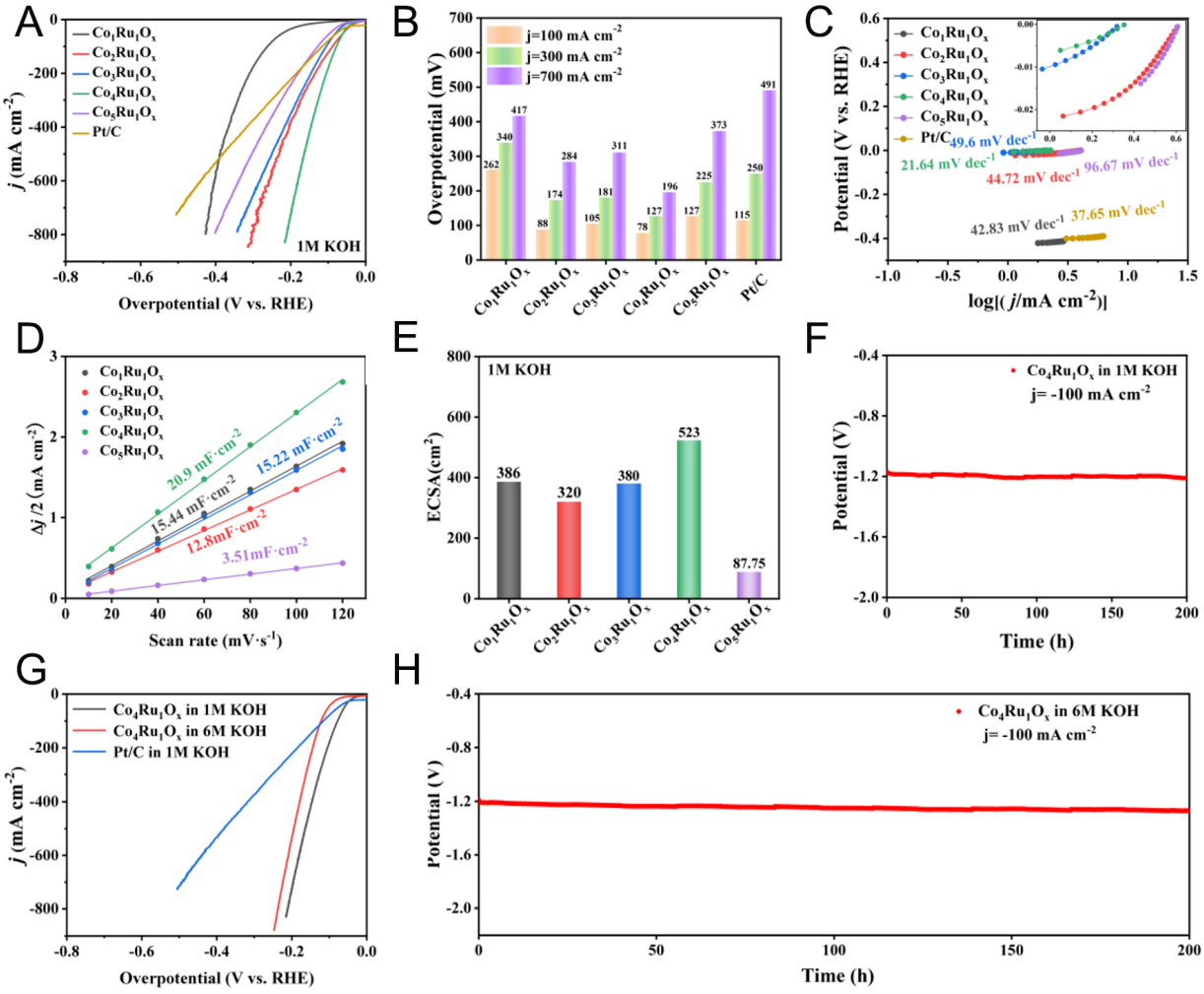

Figure 1. HER characterization of $Co_xRu_1O_x$ and reference catalysts in 1 M KOH: (A) LSV responses; (B) overpotentials at selected current densities; (C) Tafel plots; (D) C_{dl}; (E) ECSA; and (F) 200 h chronopotentiometry of $Co_4Ru_1O_x$ at -100 mA cm^{-2}. (G) HER polarization of $Co_4Ru_1O_x$ in 1 and 6 M KOH, together with Pt/C in 1 M KOH. (H) A 200 h stability trace for $Co_4Ru_1O_x$ at -100 mA cm^{-2} in 6 M KOH.

RESULTS AND DISCUSSION

Evaluation of HER performance

Alkaline HER activity was first compared for the prepared $CoRuO_x$ electrodes in 1 M KOH. $Co_4Ru_1O_x$ was the most active composition: overpotentials of 78, 127, and 196 mV produced 100, 300, and 700 mA cm^{-2}, respectively. At 100 and 300 mA cm^{-2}, these values were lower than those of $Co_1Ru_1O_x$ (262 and 340 mV), $Co_5Ru_1O_x$ (127 and 225 mV), and commercial Pt/C (115 and 250 mV) [Figure 1A and B]. Its advantage over Pt/C increased further at 700 mA cm^{-2}, supporting its suitability for high-current alkaline operation[9,24]. The Tafel plot in Figure 1C gave a slope of 21.64 mV dec^{-1} for $Co_4Ru_1O_x$, smaller than those of the other prepared electrodes and Pt/C, and therefore indicative of faster HER kinetics[25].

Cyclic voltammetry was used to probe the origin of the high HER activity. $Co_1Ru_1O_x$, $Co_2Ru_1O_x$, $Co_3Ru_1O_x$, $Co_4Ru_1O_x$, $Co_5Ru_1O_x$, and Pt/C were scanned from 10 to 120 mV s^{-1} [Supplementary Figure 1]. As presented in Figure 1D, the C_{dl} of $Co_4Ru_1O_x$ was 20.9 mF cm^{-2}, exceeding the values for $Co_5Ru_1O_x$ (3.51 mF cm^{-2}), $Co_1Ru_1O_x$ (15.44 mF cm^{-2}), and Pt/C (13.2 mF cm^{-2}; Supplementary Figure 2). The calculated ECSA values are

summarized in Figure 1E. $Co_4Ru_1O_x$ reached 523 cm^2, compared with 330 cm^2 for Pt/C, consistent with a larger number of accessible sites. Chronopotentiometry in 1 M KOH was then used to assess durability. At -100 mA cm^{-2}, the potential of $Co_4Ru_1O_x$ changed negligibly over 200 h [Figure 1F], demonstrating robust alkaline stability.

The polarization response in 6 M KOH was compared with that in 1 M KOH in Figure 1G. Larger overpotentials, especially at high current, were observed in the more concentrated electrolyte. The greater viscosity and lower water activity of 6 M KOH can impede ion diffusion, transport near the electrode, and detachment of gas bubbles[26,27]. A smaller population of free water molecules may also slow water dissociation, an important kinetic step in alkaline HER[28,29]. Thus, any conductivity gain at higher KOH concentration is offset by less favorable mass transfer and interfacial reaction conditions. Nevertheless, $Co_4Ru_1O_x$ needed only 121, 162, and 223 mV to reach 100, 300, and 700 mA cm^{-2} in 6 M KOH. In addition, operation at -100 mA cm^{-2} was maintained for 200 h [Figure 1H]. These observations demonstrate catalytic activity and long-term durability over a wide range of alkaline concentrations.

Morphologies and structures of $CoRuO_x$

Morphological, structural, and elemental data for $Co_4Ru_1O_x$ are compiled in Figure 2. Before the durability experiment, the SEM image in Figure 2A shows an interconnected, comparatively uniform porous network. This architecture increases access to reaction sites and supports electrolyte infiltration and reactant transport, which benefit HER[30]. The pre-test EDS maps [Supplementary Figure 3] show broadly even distributions of Co, Ru, Ni, and O. After 200 h of HER operation, most of the porous skeleton remains visible, although limited reconstruction and small surface particles appear [Figure 2B]. The post-test maps in Supplementary Figure 4 continue to show well-retained distributions of all four elements, with no clear sign of migration. These observations support the structural and compositional durability of $Co_4Ru_1O_x$. TEM, HRTEM, and local EDS mapping were additionally used to resolve the catalyst structure. Lattice fringes are evident in the TEM image and in enlarged HRTEM views in Figure 2C. Spacings of approximately 0.318 and 0.204 nm correspond to the RuO_2 (110) and Co_3O_4 (400) planes, respectively, confirming RuO_x- and CoO_x-related oxide domains[31,32]. The TEM image in Supplementary Figure 5 and EDS maps in Figure 2D further demonstrate good dispersion of Co, Ru, Ni, and O in the chosen region. Accordingly, the material combines locally crystalline oxide domains with homogeneous elemental dispersion.

XPS was used to compare the surface states of $Co_4Ru_1O_x$ before and after the 200 h HER test in 1 M KOH [Supplementary Figure 6]. The survey spectra in Supplementary Figure 6A contain signals from Co, Ru, O, C, and Ni in both specimens, showing that the principal surface elements persist after extended operation. In the Co 2p spectra [Supplementary Figure 6B], the initial Co $2p_{3/2}$ and Co $2p_{1/2}$ components occur at 780.9 and 796.9 eV, with satellites at 789.5 and 801.2 eV[33,34]. Following the durability test, the principal components were observed at 781.1 and 797.3 eV, and the satellites at 787.6 and 801.6 eV. The modest changes in position and line shape indicate that the Co-containing surface species remain largely intact. The O 1s spectra in Supplementary Figure 6C contain surface-oxygen and lattice-oxygen contributions. Their initial positions, 531.9 and 530.9 eV, shift to 531.4 and 530.7 eV after testing[34,35], while the two-component profile is preserved. This response is consistent with a stable oxygen environment and oxide framework. Supplementary Figure 6D covers the overlapping C 1s/Ru 3d region. Before testing, the 284.8 eV feature arises from C-C/C=C bonds, and the 280.2 and 286.6 eV components are associated with Ru 3d[36]. Ru-related signals remain readily observable after 200 h without an obvious loss in overall intensity, confirming retention of surface Ru.

The electronic states and short-range coordination of Co and Ru were probed by XPS and XAFS to understand the superior HER activity of $Co_4Ru_1O_x$. The high-resolution spectra indicate appreciable Co-Ru electronic coupling [Supplementary Figure 7]. Relative to RuO_x, the Ru $3d_{5/2}$ component shifts by about

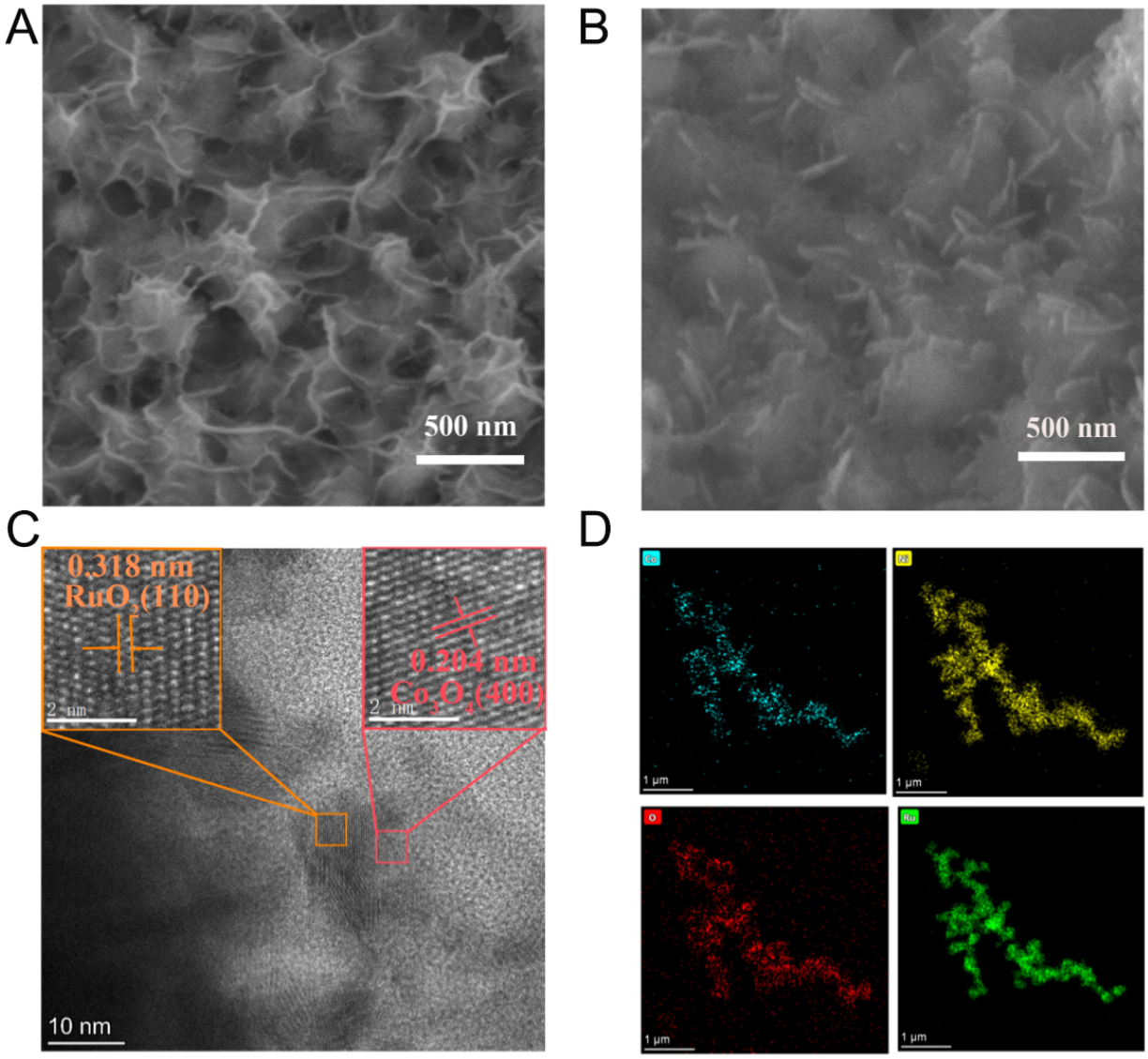

Figure 2. Morphology and elemental distribution of $Co_4Ru_1O_x$: SEM images obtained (A) before and (B) after a 200 h HER durability experiment in 1 M KOH; (C) TEM image with magnified HRTEM regions; and (D) associated EDS maps.

0.5 eV, from 280.7 to 280.2 eV, in $Co_4Ru_1O_x$. The Co $2p_{3/2}$ and Co $2p_{1/2}$ components likewise move from 781.4 and 797.5 eV in CoO_x to 780.9 and 796.9 eV in the mixed oxide, decreases of approximately 0.5 and 0.6 eV[37]. The correlated shifts support electron-density redistribution between the two metals and the formation of modified surface electronic and chemical environments after Ru is introduced[38].

Differences between the Co K-edge XANES spectra of $Co_4Ru_1O_x$ and CoO_x [Supplementary Figure 8] provide further evidence that the electronic environment of Co is altered. Fourier-transformed EXAFS also reveals a change in local coordination. CoO_x displays a principal contribution near 2.6 Å that is assigned to Co-O-Co coordination[39], whereas $Co_4Ru_1O_x$ has a feature near 1.9 Å associated with Co-M (M = Co or Ru) scattering and a weaker Co-O-Co signal. Ru addition therefore reconstructs the local environment of Co and electronically tunes the cobalt-oxide framework. Taken together, the XPS and XAFS data show that Ru changes both the electronic state and coordination of Co, producing catalytic centers with favorable

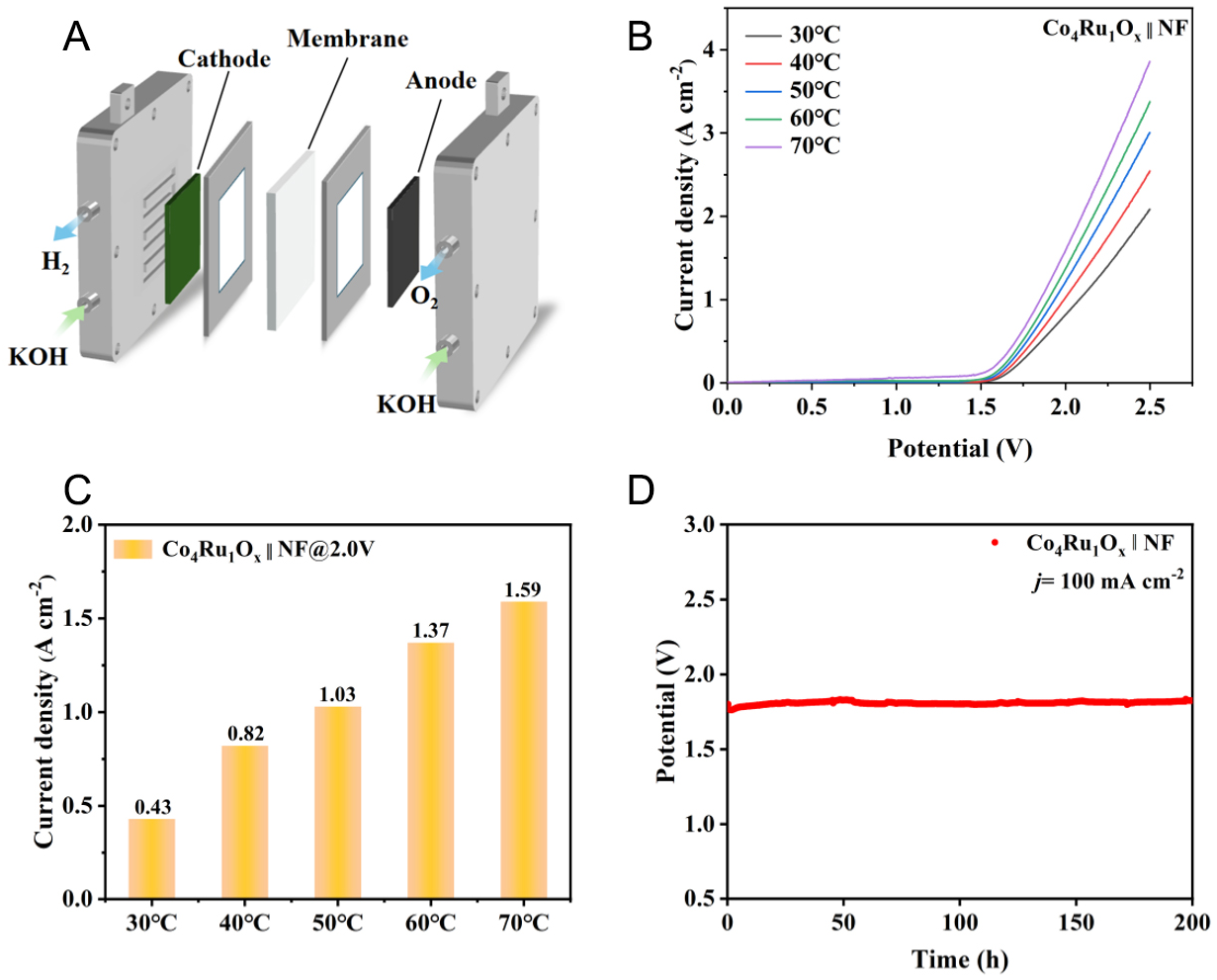

Figure 3. Performance of a $Co_4Ru_1O_x$||NF membrane electrolyzer: (A) device configuration; (B) polarization at 30-70 °C; (C) current density at 2.0 V as a function of temperature; and (D) a 200 h chronopotentiometric trace collected at 100 mA cm^{-2}.

interfacial electronic properties. This reconstruction promotes interfacial electron transfer and regulates the interaction between the active sites and hydrogen intermediates, which helps explain the high HER activity of $Co_4Ru_1O_x$.

Evaluation of MEA performance

Practical HER behavior was examined in a MEA electrolyzer[40,41]. The cathode consisted of $Co_4Ru_1O_x$ on NF, and uncoated NF was used as the anode; this device is denoted $Co_4Ru_1O_x$||NF. Figure 3A depicts its cathode-membrane-anode arrangement. Figure 3B shows polarization curves for a 1 × 1 cm^2||1 × 1 cm^2 cell at several temperatures. Increasing the temperature from 30 to 70 °C continuously increased current density, consistent with accelerated interfacial kinetics, ion transport, and gas-bubble removal. At 2.0 V, the current density rose from 0.43 A cm^{-2} at 30 °C to 1.59 A cm^{-2} at 70 °C [Figure 3C]. During a 200 h chronopotentiometric experiment at 100 mA cm^{-2}, the cell voltage remained close to 1.8 V with only small variations [Figure 3D]. The stable response demonstrates the promise of $Co_4Ru_1O_x$||NF for membrane-electrolyzer operation.

Electrochemical performance in neutral and near-neutral electrolytes

Catalyst response in neutral and near-neutral media was assessed in 1 M PBS and saturated $KHCO_3$ [Figure 4]. PBS measurements used a three-electrode arrangement with graphite and Ag/AgCl as the counter and reference electrodes. In Figure 4A and B, $Co_4Ru_1O_x$ reaches 10, 100, and 300 mA cm^{-2} at 16, 217, and

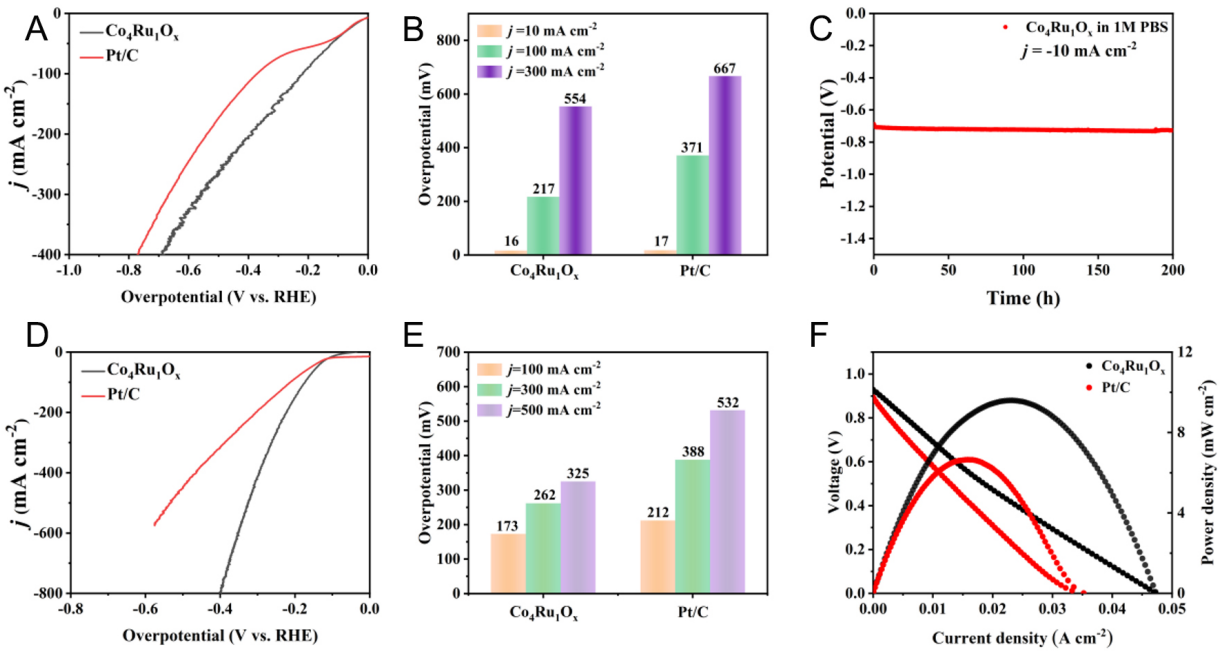

Figure 4. Neutral and near-neutral electrochemical behavior of $Co_4Ru_1O_x$: (A) HER polarization, (B) selected overpotentials, and (C) a 200 h stability trace at -10 mA cm^{-2} in 1 M PBS; (D) polarization and (E) selected overpotentials in saturated $KHCO_3$; and (F) discharge polarization/power-density profiles for Zn-CO_2 cells containing $Co_4Ru_1O_x$ or Pt/C cathodes.

554 mV, whereas Pt/C requires 17, 371, and 667 mV. The two electrodes are comparable at low current, but the mixed oxide needs substantially less overpotential at higher current[17]. The Tafel slopes are 99.51 mV dec^{-1} for $Co_4Ru_1O_x$ and 169.55 mV dec^{-1} for Pt/C [Supplementary Figure 9], again favoring the oxide catalyst. CV and C_{dl} analyses in Supplementary Figures 10-13 give 7.36 mF cm^{-2} for $Co_4Ru_1O_x$ and 12.21 mF cm^{-2} for Pt/C. Because superior high-current activity is obtained despite the smaller C_{dl}, the advantage in PBS is attributed primarily to faster reaction kinetics, more effective use of surface sites, and porous-structure-assisted mass transport. The potential remained nearly constant over 200 h at -10 mA cm^{-2} [Figure 4C], confirming durability in the phosphate buffer.

Saturated $KHCO_3$ was also examined in a three-electrode cell using graphite as the counter electrode and Hg/HgO as the reference. In this electrolyte, $Co_4Ru_1O_x$ again outperformed Pt/C. The oxide catalyst required 173, 262, and 325 mV to produce 100, 300, and 500 mA cm^{-2}, respectively, compared with 212, 388, and 532 mV for Pt/C [Figure 4D and E]. These values demonstrate effective HER operation in a near-neutral bicarbonate medium. Tafel slopes from Supplementary Figure 14 were 51.85 and 53.88 mV dec^{-1} for $Co_4Ru_1O_x$ and Pt/C, indicating similar kinetics with a small advantage for the former. Supplementary Figures 15-17 yield C_{dl} values of 20.41 and 38.51 mF cm^{-2}, respectively. Thus, the lower overpotentials of $Co_4Ru_1O_x$ cannot be explained by a larger electrochemical area; more efficient active-site utilization and reaction kinetics are the more likely origins.

Device-level utility was investigated by using $Co_4Ru_1O_x$ as the cathode catalyst in a Zn-CO_2 cell[42,43]. In the mechanism described by Kim *et al.*[20], hydration of dissolved CO_2 generates carbonic acid and produces a mildly acidic cathodic environment favorable for HER. Simultaneously, Zn oxidation at the anode supplies electrons, allowing hydrogen and electricity to be generated together. The $Co_4Ru_1O_x$-based cell attained 9.6 mW cm^{-2}, *vs.* 6.6 mW cm^{-2} for the Pt/C cell [Figure 4F]. These results extend the favorable neutral and near-neutral response observed in PBS and $KHCO_3$ to a complete Zn-CO_2 device.

Table 1. Comparison of HER performance of $Co_4Ru_1O_x$ with representative Ru-based and Co-Ru-based electrocatalysts

Electrocatalysts	Overpotential	Tafel slope	Stability	Reference
$Co_4Ru_1O_x$	η_{100} = 78 mV (1 M KOH)	21.64 mV dec^{-1}	@-100 mA cm^{-2} 200 h	This work
$RuCo_3O_4$-NiO-NF	η_{100} = 115 mV (1 M KOH)	53.9 mV dec^{-1}	@-100 mA cm^{-2} 60 h	[12]
Ru/Co_4N/NF	η_{100} = 145 mV (1 M KOH)	25 mV dec^{-1}	@-100 mA cm^{-2} 120 h	[44]
Ru-Co@Ti_2AlC	η_{100} = 95 mV (1 M KOH)	105 mV dec^{-1}	@-20 mA cm^{-2} 48 h	[45]
Ru-O-Ru clusters	η_{100} = 86 mV (1 M KOH)	29.2 mV dec^{-1}	@-100 mA cm^{-2} 50 h	[46]
$NiRuO_x$-Ar	η_{100} = 94 mV (1 M KOH)	52.73 mV dec^{-1}	@-50 mA cm^{-2} 100 h	[47]
Ru/Ni_3N-Ni	η_{100} = 135 mV (1 M KOH)	32.4 mV dec^{-1}	1,000 cycles	[48]
Ru-NiO/CNTs	η_{100} = 98 mV (1 M KOH)	56.5 mV dec^{-1}	@-10 mA cm^{-2} 100 h	[49]
RuO_2–Ti_3C_2/NF	η_{100} = 85 mV (1 M KOH)	127.5 mV dec^{-1}	@-20 mA cm^{-2} 40 h	[50]
cRu-Ni_3N/NF	η_{100} = 99 mV (1 M KOH)	26.2 mV dec^{-1}	5,000 cycles	[51]
Ru-Ni_3N@NC	η_{50} = 101 mV (1 M KOH)	70 mV dec^{-1}	@-10 mA cm^{-2} 10 h	[52]
Ru NRs/TiN	η_{100} = 150 mV (1 M KOH)	27.08 mV dec^{-1}	1,000 cycles	[53]
$Co_4Ru_1O_x$	η_{10} = 16 mV η_{100} = 217 mV (1 M PBS)	99.51 mV dec^{-1}	@-10 mA cm^{-2} 200 h	This work
Ru-WO_{3-x}/CP	η_{10} = 19 mV (1 M PBS)	41 mV dec^{-1}	@-20 mA cm^{-2} 30 h	[54]
CoRu/CoRuP	η_{10} = 31 mV (1 M PBS)	53.09 mV dec^{-1}	@-10 mA cm^{-2} 40 h	[55]

Table 1 benchmarks $Co_4Ru_1O_x$ against recent Ru- and Ru-Co-containing HER electrocatalysts in terms of overpotential, Tafel slope, electrolyte, test current, and durability. In 1 M KOH, $Co_4Ru_1O_x$ combines an overpotential of 78 mV at -100 mA cm^{-2}, a 21.64 mV dec^{-1} Tafel slope, and 200 h of continuous operation. This balance of activity and durability compares favorably with many reported Ru-based and Ru-Co-based materials and is consistent with cooperative Co/Ru oxide effects and a tuned surface electronic environment. Unlike most alkaline-centered reports, the present catalyst also remains active in neutral PBS and bicarbonate media, demonstrating compatibility with distinct proton-transfer environments.

Electrochemical impedance spectroscopy was used to clarify why $Co_4Ru_1O_x$ remains highly active even though its C_{dl} is lower than that of Pt/C in PBS and saturated $KHCO_3$ (Nyquist plots, Supplementary Figure 18). The solution resistances (R_s) of $Co_4Ru_1O_x$ and Pt/C are 1.44 and 1.92 Ω in 1 M KOH, 4.06 and 5.83 Ω in 1 M PBS, and 1.52 and 2.25 Ω in saturated $KHCO_3$, respectively. Although R_s varies with electrolyte conductivity, its consistently smaller value for the mixed oxide indicates lower ohmic losses under each HER condition.

Operando Raman spectra were next collected in 1 M KOH, 1 M PBS, and saturated $KHCO_3$ to probe the HER interface [Supplementary Figure 19]. Similar potential-dependent changes in the broad O-H stretching envelope near 3,500 cm^{-1} appear in all three media, showing that interfacial water activation is retained. The

elementary HER sequence is comparable, but its rate is shaped by electrolyte-specific proton donors, conductivity, and interfacial solvation. In KOH, water dissociation precedes formation of adsorbed hydrogen. The near-neutral PBS environment supplies fewer protons and normally slows proton transfer; nevertheless, effective water activation at $Co_4Ru_1O_x$ supports proton delivery and HER[54]. In saturated $KHCO_3$, bands near 1,015 and 1,064 cm^{-1} are assigned to HCO_3^- and CO_3^{2-}, respectively[56,57], evidencing a dynamic interfacial bicarbonate/carbonate equilibrium that buffers local proton transfer. The absence of new bands associated with heavy carbonate or bicarbonate accumulation suggests that these species do not substantially obstruct the active interface. FTIR spectra in Supplementary Figure 20 show hydroxyl-stretching and water-bending bands near 3,404 and 1,630 cm^{-1}, respectively, for both RuO_x and $Co_4Ru_1O_x$[58]. The stronger hydroxyl-related absorption of the mixed oxide indicates greater interaction with interfacial water. Its electrolyte tolerance therefore derives from maintained water activation together with effective charge and proton transport, rather than from identical kinetics in every electrolyte.

CONCLUSIONS

A porous $Co_4Ru_1O_x$ electrode was prepared on three-dimensional NF by co-precipitation and calcination and evaluated under several HER conditions. Tuning the Co/Ru ratio enhanced activity, kinetics, and durability through cooperative Co/Ru oxide chemistry, efficient electron and ion transport within the NF network, and ready access to surface sites. After prolonged electrolysis, the porous architecture and homogeneous elemental distribution were largely retained, demonstrating structural and compositional resilience. A MEA containing $Co_4Ru_1O_x$||NF operated continuously for 200 h at 100 mA cm^{-2}, supporting its use in practical water splitting. In addition to strong alkaline performance, the catalyst responded effectively and stably in PBS and saturated $KHCO_3$, confirming adaptability to neutral and near-neutral media. Its promising power output in a Zn-CO_2 cell further broadens the potential applications beyond water electrolysis. Overall, the findings connect composition control and porous-electrode design with multi-environment operation and provide a route toward versatile, high-performance Ru-Co oxide electrocatalysts.

DECLARATIONS

Authors' contributions

Investigation, formal analysis, writing - original draft: Zheng, Q.
Data curation, investigation: Li, Y.
Validation, formal analysis: Lu, C.
Writing - review & editing: Maubane-Nkadimeng, M. S.
Supervision, funding acquisition, writing - review & editing: Feng, T.
Conceptualization, project administration, resources: Niu, B.
All authors read and approved the final manuscript.

Availability of data and materials

The data supporting the findings of this study are available in the article and its Supplementary Materials. Additional raw data are available from the corresponding author upon reasonable request.

AI and AI-assisted tools statement

During the preparation of this manuscript, the AI tool ChatGPT (GPT-5.5 Instant, released 2026-05-05) was used to assist with language editing and manuscript refinement. In addition, ChatGPT Images 2.0 (released 2026-04-21) was used to assist in creating the graphical abstract. After using this tool/service, the authors carefully reviewed and edited the generated content as needed and take full responsibility for the content of the published article.

Financial support and sponsorship

This work was supported by the National Natural Science Foundation of China (No. W2441008) and the Natural Science Foundation of Liaoning (LJ212510146025).

Conflicts of interest

All authors declared that there are no conflicts of interest.

Ethical approval and consent to participate

Not applicable.

Consent for publication

Not applicable.

Supplementary Materials

Supplementary Materials

REFERENCES

1. Shi, J.; Wang, M.; Peng, L.; et al. Engineered Mo-O-Fe active centers for Efficient and stable overall water splitting along the lattice-oxygen mechanism. *Green. Energy. Environ.* **2026**, S2468025726000464. DOI
2. Sazali, N. Emerging technologies by hydrogen: a review. *Int. J. Hydrogen. Energy.* **2020**, *45*, 18753-71. DOI
3. Yang, X.; Luo, X.; Zhou, Y.; et al. Synergistic optimization of pore structure and hydrophilicity for an ultrathin, high-safety composite diaphragm toward high-current, durable alkaline water electrolysis. *Sci. Bull.* **2026**, *71*, 3937-50. DOI
4. He, J.; He, Y.; Liu, X.; et al. Beyond oxygen evolution: recent progress in hydrogen production via anodic substitution reactions. *Mater. Rep. Energy.* **2026**, *6*, 100426. DOI
5. Zhao, C.; Li, H.; Li, F. Diverging maturity and converging challenges of water and CO_2 electrolysis in 2025. *Nat. Rev. Clean. Technol.* **2026**, *2*, 8-10. DOI
6. Lee, Y.; Theerthagiri, J.; Sahu, B. K.; Jeon, I.; Shin, H.; Choi, M. Y. Pulsed laser-engineered single-atom Pt sites on MoC for unprecedented alkaline hydrogen evolution over acidic media. *Mater. Rep. Energy.* **2026**, *6*, 100403. DOI
7. Hou, L.; Jang, H.; Gu, X.; et al. Design strategies of ruthenium-based materials toward alkaline hydrogen evolution reaction. *EcoEnergy* **2023**, *1*, 16-44. DOI
8. Wu, L.; Wang, Q.; Li, W.; Tang, M.; An, L. Multi-scale modeling of the multi-phase flow in water electrolyzers for green hydrogen production. *Mater. Rep. Energy.* **2025**, *5*, 100356. DOI
9. Zhu, Y.; Klingenhof, M.; Gao, C.; et al. Facilitating alkaline hydrogen evolution reaction on the hetero-interfaced Ru/RuO_2 through Pt single atoms doping. *Nat. Commun.* **2024**, *15*, 1447. DOI PubMed PMC
10. Lin, B.; Chen, X.; Niu, B.; Lin, Y.; Chen, Y.; Lin, X. The research progress of ruthenium-based catalysts for the alkaline hydrogen evolution reaction in water electrolysis. *Catalysts* **2024**, *14*, 671. DOI
11. Yu, X.; Qi, R.; Zhang, L.; et al. Ruthenium-cobalt oxide solid solution nanofiber: a robust bifunctional electrocatalyst for overall water splitting with superior ampere-grade-current-density electrocatalytic performance. *Acta. Mater.* **2025**, *294*, 121165. DOI
12. Zhang, H.; Guo, H.; Ren, J.; Jin, X.; Li, X.; Song, R. Synergistic engineering of morphology and electronic structure in constructing metal-organic framework-derived Ru doped cobalt-nickel oxide heterostructure towards efficient alkaline hydrogen evolution reaction. *Chem. Eng. J.* **2021**, *426*, 131300. DOI
13. Ren, F.; Xu, J.; Feng, L. An effective bimetallic oxide catalyst of RuO_2-Co_3O_4 for alkaline overall water splitting. *Nano. Res.* **2023**, *17*, 3785-93. DOI
14. Hu, L.; Han, Z.; Chen, Y.; et al. Constructing the confined RuCo nanoalloys with modulated d-band centers for efficient pH-robust hydrogen evolution. *J. Energy. Chem.* **2026**, *116*, 58-68. DOI
15. Zhou, Y.; Mao, Y.; Ye, C.; et al. Ru single atoms anchored on Co_3O_4 nanorods for efficient overall water splitting under pH-universal conditions. *Adv. Energy. Mater.* **2025**, *15*, 2500700. DOI
16. Kityk, A.; Sadeghi, B.; Pavlik, V.; Hnatko, M.; Balog, M. Unveiling structure-performance relationships in HER catalysts for sustainable and scalable hydrogen production. *Mater. Rep. Energy.* **2026**, *6*, 100407. DOI
17. Luo, J.; Zheng, J.; Wu, M.; et al. Local microenvironment reactive zone engineering promotes water activation. *Mater. Rep. Energy.* **2025**, *5*, 100327. DOI
18. Zhang, Y.; Feng, B.; Tian, J.; et al. Lattice-hydrogen cycling mechanism enables pH-universal hydrogen evolution at ampere-level current densities. *Nat. Commun.* **2025**, *16*, 10863. DOI PubMed PMC

19. Gupta, D.; Mao, J.; Guo, Z. Bifunctional catalysts for CO_2 reduction and O_2 evolution: a pivotal for aqueous rechargeable Zn-CO_2 batteries. *Adv. Mater.* **2024**, *36*, 2407099. DOI
20. Kim, C.; Kim, J.; Joo, S.; et al. Highly efficient CO_2 utilization via aqueous zinc- or aluminum-CO_2 systems for hydrogen gas evolution and electricity production. *Angew. Chem. Int. Ed.* **2019**, *58*, 9506-11. DOI PubMed
21. Kawashima, K.; Márquez, R. A.; Son, Y. J.; et al. Accurate potentials of Hg/HgO electrodes: practical parameters for reporting alkaline water electrolysis overpotentials. *ACS. Catal.* **2023**, *13*, 1893-8. DOI
22. Li, Y.; Wang, S.; Yuan, M.; et al. Piezoelectric activation of dual lattice-oxygen mechanism through OH- Grotthuss transport in water electrolysis. *Nat. Commun.* **2026**, *17*, 4346. DOI PubMed PMC
23. Mccrory, C. C. L.; Jung, S.; Peters, J. C.; Jaramillo, T. F. Benchmarking heterogeneous electrocatalysts for the oxygen evolution reaction. *J. Am. Chem. Soc.* **2013**, *135*, 16977-87. DOI PubMed
24. Yao, R.; Sun, K.; Zhang, K.; et al. Stable hydrogen evolution reaction at high current densities via designing the Ni single atoms and Ru nanoparticles linked by carbon bridges. *Nat. Commun.* **2024**, *15*, 2218. DOI PubMed PMC
25. Der Zalm JM, Quintal J, Hira SA, Chen S, Chen A. Recent trends in electrochemical catalyst design for hydrogen evolution, oxygen evolution, and overall water splitting. *Electrochim. Acta.* **2023**, *439*, 141715. DOI
26. Deng, L.; Jin, L.; Yang, L.; et al. Bubble evolution dynamics in alkaline water electrolysis. *eScience* **2025**, *5*, 100353. DOI
27. Araújo, F.; Neto, R. C.; Moita, A. S. Alkaline water electrolysis: ultrasonic field and hydrogen bubble formation. *Int. J. Hydrogen. Energy.* **2024**, *78*, 594-603. DOI
28. Chang, B.; Liu, X.; Zuo, S.; et al. Dynamic construction of a durable epitaxial catalytic layer for industrial alkaline water splitting. *Nat. Commun.* **2025**, *16*, 7959. DOI PubMed PMC
29. Zhou, S.; Cao, W.; Shang, L.; et al. Facilitating alkaline hydrogen evolution kinetics via interfacial modulation of hydrogen-bond networks by porous amine cages. *Nat. Commun.* **2025**, *16*, 1849. DOI PubMed PMC
30. Jiang, X.; Kyriakou, V.; Song, C.; et al. A novel multi-channel porous structure facilitating mass transport towards highly efficient alkaline water electrolysis. *J. Energy. Chem.* **2024**, *93*, 511-8. DOI
31. Ping, X.; Liu, Y.; Zheng, L.; et al. Locking the lattice oxygen in RuO_2 to stabilize highly active Ru sites in acidic water oxidation. *Nat. Commun.* **2024**, *15*, 2501. DOI PubMed PMC
32. Yao, T.; Guo, X.; Qin, S.; et al. Effect of rGO coating on interconnected Co_3O_4 nanosheets and improved supercapacitive behavior of Co_3O_4/rGO/NF architecture. *Nano. Micro. Lett.* **2017**, *9*, 38. DOI PubMed PMC
33. Laïk, B.; Richet, M.; Emery, N.; et al. XPS investigation of Co-Ni oxidized compounds surface using peak-on-satellite ratio. Application to $Co_{20}Ni_{80}$ passive layer structure and composition. *ACS. Omega.* **2024**, *9*, 40707-22. DOI PubMed PMC
34. Thomas, B.; Peng, B.; Huang, X.; Asefa, T. Improving the electrocatalytic activity of cobalt oxide with bismuth for acidic oxygen evolution reaction. *J. Mater. Chem. A.* **2024**, *12*, 22528-38. DOI
35. Yang, Y.; Xu, Y.; Liu, H.; et al. Unraveling the modulation essence of p bands in Co-based oxide stability on acidic oxygen evolution reaction. *Nano. Res.* **2024**, *17*, 5922-9. DOI
36. Wang, Z.; Song, C.; Shen, H.; Ma, S.; Li, G.; Li, Y. RuO_x quantum dots loaded on graphdiyne for high-performance lithium-sulfur batteries. *Adv. Mater.* **2023**, *36*, 2307786. DOI
37. Yang, Y.; Wang, L.; Ma, M.; et al. Synergistic interface engineering of RuO_2/Co_3O_4 heterostructures for enhanced overall water splitting in acidic media. *Adv. Energy. Sustain. Res.* **2023**, *4*, 2300057. DOI
38. Tan, L.; Zhang, A.; Liu, Z.; et al. Nanostructured RuO_2-Co_3O_4@RuCo-EO with low Ru loading as a high-efficiency electrochemical oxygen evolution catalyst. *RSC. Adv.* **2021**, *11*, 11779-85. DOI PubMed PMC
39. Jiao, J.; Zhang, N. N.; Zhang, C.; et al. Doping ruthenium into metal matrix for promoted pH-universal hydrogen evolution. *Adv. Sci.* **2022**, *9*, 2200010. DOI PubMed PMC
40. Lee, J. K.; Seo, J. H.; Lim, J.; Park, S.; Jang, H. W. Best practices in membrane electrode assembly for water electrolysis. *ACS. Mater. Lett.* **2024**, *6*, 2757-86. DOI
41. Jeon, S. S.; Lee, W.; Jeon, H.; Lee, H. Developing catalysts for membrane electrode assemblies in high performance polymer electrolyte membrane water electrolyzers. *ChemSusChem* **2024**, *17*, e202301827. DOI PubMed PMC
42. Liu, Y.; An, Y.; Zhu, J.; et al. Integrated energy storage and CO_2 conversion using an aqueous battery with tamed asymmetric reactions. *Nat. Commun.* **2024**, *15*, 977. DOI PubMed PMC
43. Wang, H.; Aslam, M. K.; Nie, Z.; et al. Dual-anion regulation for reversible and energetic aqueous Zn-CO_2 batteries. *Small. Methods.* **2023**, *8*, 2300867. DOI
44. Xing, M.; Guo, X.; Yuan, W.; et al. Realization of electron-deficient Ru sites *via* Co_4N coupling for synergistically enhanced alkaline hydrogen evolution. *J. Mater. Chem. A.* **2023**, *11*, 22147-53. DOI

45. Kutyła, D.; Krstajić, Pajić. M. N.; Lačnjevac, UČ.; Marzec, M. M.; Elezović, N. R.; Żabiński, P. Ru-Co alloy coatings electrodeposited on a MAX phase substrate as efficient catalysts for the hydrogen evolution reaction. *Int. J. Hydrogen. Energy.* **2024**, *56*, 28-40. DOI
46. Liu, D.; Xu, L.; Li, S.; et al. Atomically precise Ru-O-Ru clusters for enhanced water dissociation in alkaline hydrogen evolution. *Nano. Res.* **2024**, *17*, 6993-7000. DOI
47. Xu, N.; Li, M.; Sun, H.; et al. Atmosphere-driven oriental regulation of Ru valence for boosting alkaline water electrolysis. *Chem. Eng. J.* **2024**, *502*, 158051. DOI
48. Liu, Z.; Zha, M.; Wang, Q.; Hu, G.; Feng, L. Overall water-splitting reaction efficiently catalyzed by a novel bi-functional Ru/Ni_3 N-Ni electrode. *Chem. Commun.* **2020**, *56*, 2352-5. DOI
49. Chen, Y.; Lee, Y.; Chu, W.; Li, J. Trace Ru-tuned NiO/CNT electrocatalysts outperform benchmark Pt for alkaline hydrogen evolution with superior mass activity. *Chem. Eng. J.* **2023**, *472*, 144922. DOI
50. Zhang, Y.; Zhang, Z.; Yu, Z.; et al. Ruthenium oxide nanoparticles immobilized on Ti_3C_2 MXene nanosheets for boosting seawater electrolysis. *ACS. Appl. Mater. Interfaces.* **2023**, *15*, 58345-55. DOI
51. Zhu, J.; Lu, R.; Shi, W.; et al. Epitaxially grown Ru clusters-nickel nitride heterostructure advances water electrolysis kinetics in alkaline and seawater media. *Energy. Environ. Mater.* **2022**, *6*, e12318. DOI
52. Liu, Y.; Zheng, D.; Zhao, Y.; et al. Ru-doped 3D porous Ni_3N sphere as efficient Bi-functional electrocatalysts toward urea assisted water-splitting. *Int. J. Hydrogen. Energy.* **2022**, *47*, 25081-9. DOI
53. Yang, Y.; Wu, D.; Li, R.; et al. Engineering the strong metal support interaction of titanium nitride and ruthenium nanorods for effective hydrogen evolution reaction. *Appl. Catal. B. Environ.* **2022**, *317*, 121796. DOI
54. Chen, J.; Chen, C.; Qin, M.; et al. Reversible hydrogen spillover in Ru-WO_{3-x} enhances hydrogen evolution activity in neutral pH water splitting. *Nat. Commun.* **2022**, *13*, 5382. DOI PubMed PMC
55. Yao, R.; Wu, Y.; Zhang, K.; et al. Construction of a CoRu/CoRuP heterogeneous electrocatalyst for efficient pH-universal hydrogen production. *ACS. Sustain. Chem. Eng.* **2023**, *12*, 291-9. DOI
56. Wu, Q.; Yang, N.; Xiao, M.; Wang, W.; Cui, C. Bicarbonate-mediated proton transfer requires cations. *Nat. Commun.* **2024**, *15*, 9145. DOI PubMed PMC
57. Zhang, Y.; Pan, B.; Li, Y.; Wang, Y. Electrochemical pH-swing CO_2 capture facilitated by suppressed bubble accumulation at electrode/electrolyte interfaces. *Angew. Chem. Int. Ed.* **2025**, *65*, e13456. DOI
58. Sun, K.; Wu, X.; Zhuang, Z.; et al. Interfacial water engineering boosts neutral water reduction. *Nat. Commun.* **2022**, *13*, 6260. DOI PubMed PMC